Photochemistry of CH₃Cl: Dissociation and CH···Cl Hydrogen Bond Formation

Vanessa C. de Medeiros,[†] Railton B. de Andrade,[†] Ezequiel F. V. Leitão,[†] Elizete Ventura,[†] Glauco F. Bauerfeldt,[‡] Mario Barbatti,*,[§] and Silmar A. do Monte*,[†]

[†]Departamento de Química, CCEN, Universidade Federal da Paraíba, João Pessoa, PB 58059-900, Brazil

[‡]Departamento de Química, Instituto de Ciências Exatas, UFRRJ, Pavilhão Roberto Alvahydo (PQ), sala 44. km 7, Rodovia Br 465, Seropédica, RJ 23890-000, Brazil

[§]Aix Marseille Université, CNRS, ICR UMR7273, 13397 Marseille, France

Ⓢ *Supporting Information*

ABSTRACT: State-of-the-art electronic structure calculations (MR-CISD) are used to map five different dissociation channels of CH_3Cl along the C−Cl coordinate: (i) $CH_3(\tilde{X}^2A_2'') + Cl(^2P)$, (ii) $CH_3(3s^2A_1') + Cl(^2P)$, (iii) $CH_3^+(^1A_1') + Cl^-(^1S)$, (iv) $CH_3(3p^2E') + Cl(^2P)$, and (v) $CH_3(3p^2A_2'') + Cl(^2P)$. By the first time these latter four dissociation channels, accessible upon VUV absorption, are described. The corresponding dissociation limits, obtained at the MR-CISD+Q level, are 3.70, 9.50, 10.08, 10.76, and 11.01 eV. The first channel can be accessed through $n\sigma^*$ and n3s states, while the second channel can be accessed through n_e3s, n_e3p_σ, and $\sigma3s$ states. The third channel, corresponding to the $CH_3^+ + Cl^-$ ion-pair, is accessed through n_e3p_e states. The fourth is accessed through n_e3p_e, n_e3p_σ, and $\sigma3p_\sigma$, while the fifth through $\sigma3p_e$ and $\sigma_{CH}\sigma^*$ states. The population of the diverse channels is controlled by two geometrical spots, where intersections between multiple states allow a cascade of nonadiabatic events. The ion-pair dissociation occurs through formation of $CH_3^+···Cl^-$ and $H_2CH^+···Cl^-$ intermediate complexes bound by 3.69 and 4.65 eV. The enhanced stability of the $H_2CH^+···Cl^-$ complex is due to a CH···Cl hydrogen bond. A time-resolved spectroscopic setup is proposed to detect those complexes.
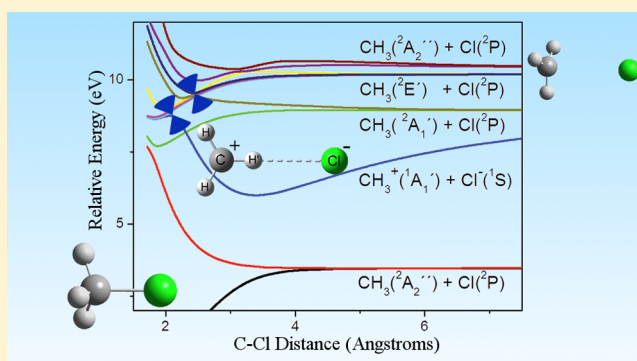
INTRODUCTION

As it is well-known, Cl atoms catalyze O_3 decomposition.[1,2] Thus, a detailed mapping of its sources is a fundamental environmental issue. In the stratosphere, these atoms are significantly generated from photolysis of methyl chloride (CH_3Cl), making this compound particularly important for atmospheric photochemistry.[3,4]

The lowest photodissociation channel of clorofluorcarbons (CFCs) and halocarbons usually involves excitations from chlorine lone pairs (n) into C−Cl antibonding (σ^*) orbitals[5−7] induced by UVB or low UVC radiation.[8] Although a large percentage of these molecules photodissociate in the stratosphere via this low-lying channel, the surviving molecules can reach the ionosphere, where vacuum UV (VUV) opens new dissociation channels after excitation into higher states.[9] Moreover, because some of these high excitations have large transition moments,[10,11] the action spectrum is shifted to high energies, making them specially relevant from the photochemical point of view.

The photodissociation of CH_3Cl has been studied at 193.3,[12,13] 157.6,[14−19] and 121.6 nm.[13,20] While the first two excitation wavelengths yield $CH_3 + Cl$ as the main photo-products, the latter also leads to the generation of H atoms with high yields. Excitation at 193.3 nm (6.41 eV) is expected to reach the long-wavelength absorption limit of the $n\sigma^*$ band,[21] while at 157.6 nm (7.87 eV) it should reach a region of much larger absorption cross section, already belonging to the n3s band.[21,22]

Apart from the well-known photodissociation channels forming neutral fragments, Tuckett et al.[23,24] measured the cross sections for Cl^- generation following photoexcitation of CH_3Cl in the range from 8 to 35 eV and obtained the most intense peak in the region from 10.5 to 11.9 eV. Moreover, this peak is much more intense than that reported for CH_2Cl^- formation.[23,24] According to a detailed analysis of the photoabsorption spectrum of CH_3Cl in the region from 6 to 12 eV provided by Locht et al.,[11] the Cl^- peak should correspond to *ns*, *np*, and *nd* Rydberg states. Previous high-level calculations at the MR-CISD+Q level indicate that the $\sigma3s$ and $\sigma3p$ Rydberg states lie in the region from ∼11 to 12 eV,[22] matching the Cl^- peak.[23,24]

Given the relevance of methyl chloride for atmospheric photochemistry, it is somewhat surprising how little theoretical information is available about its photodissociative processes. Apart from the study of Granucci et al.,[7] in which potential energy surfaces for the first three singlet states of CH_3Cl have been calculated at the CASPT2 level, theoretical reports concerning the photochemical mechanisms of CH_3Cl fragmentation in the upper atmosphere are scarce.

In this work, we aim at filling this knowledge gap by a thorough description of the main photodissociation channels of methyl chloride into $CH_3 + Cl$ and $CH_3^+ + Cl^-$. High-level ab initio potential energy profiles for a dozen singlet excited states are computed along the dissociation coordinate, comprising essentially the same energy range we have studied previously, but limited to the Franck−Condon region.[22] Strong multi-reference character, very diffuse Rydberg states, diverse avoided crossings, exotic complexes, and five different dissociation channels compose the intricate electronic structure emerging from this study. Naturally, the description of these channels requires a deep degree of technicality. We have, however, made a great effort to rationalize all this information in terms of a simple picture where CH_3Cl relaxes through a cascade of nonadiabatic processes taking place in two geometrical spots featuring multiple conical intersections, and feeding the dissociation channels on the way down, during the relaxation. This picture is possibly shared by Cl dissociation in many other CFCs and halocarbons.

Along one of these dissociation channels, we show that Cl^- production is associated with strongly bound $CH_3^+\cdots Cl^-$ and $H_2CH^+\cdots Cl^-$ intermediate complexes. We discuss below that the latter one, in particular, is stabilized by a $CH\cdots Cl$ hydrogen bond. $CH\cdots Cl$ hydrogen bonds are odd chemical structures. They have been almost exclusively reported in the solid state,[25−28] where steric effects hold the complexes together. They are invariably weak, with the H−Cl distance approximately corresponding to the sum of H and Cl van der Waals radii (3.0 Å). Searching over thousands of entries in the Cambridge Structural Database, this distance is never inferior to 2.4 Å.[26−28] $CH\cdots Cl$ hydrogen bonds may also occur aided by metallic bonds[29] or by trapping the Cl within the cavities of macromolecules.[30,31] In the present case of the $H_2CH^+\cdots Cl^-$ complex, we have not only found out that a $CH\cdots Cl$ double-charge-assisted hydrogen bond may occur in the gas phase, but also—which is even more astonishing—that it may be very strong, with a bond distance of only 1.9 Å.

■ COMPUTATIONAL DETAILS

In most of the calculations, the C_s symmetry has been used and the symmetry plane corresponds to the yz plane. The 3p lone pair of the Cl atom, which is along the C−Cl bond, has been named $3p_\sigma$. It interacts with the $2p_\sigma$ orbital of the CH_3 moiety to yield the σ_{CCl} and σ_{CCl}^* orbitals, hereafter referred as σ and σ^*. The degenerate lone pairs $(3p_x, 3p_y)$ are simply designated as n_e. Three valence (σ_{CH}) orbitals of CH_3, as well as the 3s(C), $3p_\sigma$(C), and $3p_e$(C) Rydberg orbitals, have also been included in the present study. The $n = 3$ notation for the Rydberg orbitals has been chosen on the basis of that of Rogers et al.,[23] Antol et al.,[32] and Medeiros et al.[22]

For the muticonfigurational self-consistent (MCSCF) calculations, a valence complete active space (CAS) was chosen with 12 electrons (four from the n_e orbitals, two from the σ bond, and six from the σ_{CH} orbitals) and seven orbitals (the n_e orbitals, σ and σ^*, and the three valence σ_{CH} orbitals). These valence orbitals have been included following the results of Mebel and Lin,[33] which reported a valence state between the two 3p states of CH_3. Besides, inclusion of these

orbitals is crucial to guarantee a flexible occupied space and keep the correct shape of the high-lying 3p(C) Rydberg orbitals upon dissociation. Four Rydberg orbitals (3s(C), $3p_\sigma$(C), $3p_e$(C)) have been included in the auxiliary (AUX) space and only single CAS → AUX excitations were allowed. Eleven singlet states with equal weights have been included in the state-averaged MCSCF calculations. As C_s symmetry has been used and the actual symmetry along the potential energy curves is C_{3v} one needs to compute the average energies of the correct pairs of A′ and A″ roots to get the energies of the E states. At the equilibrium geometry the correspondences are $1^1A_1 − 1^1A'$; $1^1E − (2^1A' + 1^1A'')$; $2^1E − (3^1A' + 2^1A'')$; $2^1A_1 − 4^1A'$; $3^1E − (5^1A' + 3^1A'')$; $1^1A_2 − 4^1A''$; $4^1E − (6^1A' + 5^1A'')$; $3^1A_1 − 7^1A'$; $4^1A_1 − 8^1A'$; $5^1E − (9^1A' + 6^1A'')$; $5^1A_1 − 10^1A'$.

For the multireference configuration interactions calculations with singles and doubles (MR-CISD), a slightly different orbital scheme for generating the reference configuration state functions (CSF) has been used; that is, the three σ_{CH} orbitals are included in the restricted active space (RAS). The n_e, σ, and σ^* orbitals have been included in the CAS space, while the 3s(C), $3p_\sigma$(C), $3p_e$(C) Rydberg orbitals are in the auxiliary (AUX) space. Only single RAS → CAS and CAS → AUX excitations are allowed. The total CSF space was built through single and double excitations from all internal (active + doubly occupied) into all virtual orbitals. On the basis of previous results obtained for the CF_3Cl molecule,[5,6] the K + L shells of Cl atom along with the K shell of C atom were kept frozen in all MR-CISD calculations. The interactive space restriction[34] approach has been used at this latter level.

Size-extensivity corrections have been taken into account by the generalized Davidson method (MR-CISD+Q).[35,36] The COLUMBUS program system[37−40] was used for all calculations. The atomic orbitals (AO) integrals and AO gradient integrals were calculated through program modules taken from DALTON.[41] The aug-cc-pVXZ (X = D,T) basis sets for H and Cl and the d-aug-cc-pVXZ (X = D,T) basis set for C[42−45] have been used. The d-aug basis set has been chosen centered on the C atom as the Rydberg orbitals become more localized on CH_3 fragment as the C−Cl distance increases.

The geometries along the potential energy curves have been partially optimized for the ground state (relaxed scan along the C−Cl distance) at the MR-CISD level using only the n_e, σ, and σ^* orbitals in the CAS space at both MCSCF and MR-CISD levels. The potential energy curves consist of single-point calculations at these geometries, performed using the aforementioned CAS → AUX and the RAS → CAS → AUX orbitals schemes at the MCSCF and MR-CISD levels, respectively. The potential energy curves have been computed with the mixed aug-cc-pVDZ (H,Cl)/d-aug-cc-pVDZ(C) and aug-cc-pVTZ-(H,Cl)/d″-aug′-cc-pVTZ(C) basis sets, where d″-aug′ refers to double augmentation of the cc-pVTZ basis set for carbon atom, without f function in the aug- set and without one d and one f functions in the d-set.

Dissociation limits have been calculated by performing single-point calculation using the supermolecule approach for a CH_3−Cl distance of 50 Å with the aug-cc-pVTZ(H,Cl)/d-aug-cc-pVTZ(C) basis set.

Additional full geometry optimizations at the MR-CISD level have been performed for the $CH_3^+\cdots Cl^-$ and $H_2CH^+\cdots Cl^-$ complexes as well as for the conical intersection between the $n_e\sigma^*$ and n_e3s states with the aug-cc-pVTZ(H,Cl)/d-aug-cc-pVTZ(C) basis set. In these cases, the σ_{CH} orbitals have been left in the doubly occupied space, while the CAS space is the same as that used for generating the geometries in the relaxed scan. For the conical intersection only one Rydberg orbital (3s(C)) has been included in the AUX space, while for the complexes no Rydberg orbital has been used. Such choice is justified by the high relative energies of the remaining states at these geometries. Moreover, geometry optimizations for the ground state as well as frequencies calculations have been performed for CH_3Cl, CH_3, and CH_3^+ at the same level. For CH_3Cl only the valence n_e(Cl), σ, and σ^* orbitals have been included in the CAS space at both MCSCF (the lowest three valence states have been averaged) and MR-CISD levels. For methyl radical, the three σ_{CH} and the $2p_\sigma$ orbitals have been included in the CAS space, while the four Rydberg orbitals (3s(C) and 3p(C)) are in the AUX space at both levels. As before, only single CAS

Table 1. Configuration Weights and Vertical Excitation Energies (in eV) at the MR-CISD and MR-CISD+Q Levels[a]

	weights[b]	vertical excitation energies				previous results[c]	experimental[d]
		MR-CSID	MR-CISD+Q	MR-CISD	MR-CISD+Q		
		d-aug-DZ[e]		d-aug-TZ[f]			
1^1A_1	(0.86)gs	0.00	0.00	0.00	0.00	0.00	0.00
1^1E	$(0.54)n_e\sigma^* + (0.24)n_e3s(C)$	7.53	7.56	7.52(0.002)[g]	7.51	7.51	7.25
2^1E	$(0.46)n_e3s(C) + (0.36)n_e3p_\sigma(C)$	7.75	7.84	7.80 (0.060)	7.90	7.89	7.75
2^1A_1	$(0.86)n_e3p_e(C)$	8.64	8.84	8.70 (0.004)	8.90	8.88	8.82
3^1E	$(0.88)n_e3p_e(C)$	8.65	8.85	8.71 (0.022)	8.92	8.90	8.89
1^1A_2	$(0.88)n_e3p_e(C)$	8.70	8.90	8.76 (0.000)	8.96	8.95	–
4^1E	$(0.44)n_e3p_\sigma(C)+(0.27)n_e\sigma^*+(0.17)n_e3s(C)$	9.33	9.32	9.32 (0.041)	9.32	9.31	9.20
3^1A_1	$(0.81)\sigma3s(C)$	10.91	10.99	10.90 (0.031)	10.97	10.96	–
4^1A_1	$(0.71)\sigma3p_\sigma(C)+ (0.15)\sigma\sigma^*$	11.42	11.42	11.43 (0.340)	11.42	11.40	11.64
5^1E	$(0.86)\sigma3p_e(C)$	11.87	12.01	11.87 (0.035)	12.00	11.98	11.75
5^1A_1	$(0.73)\sigma_{CH}\sigma^*$	12.83	11.57	12.90	11.87	–	–

[a]Oscillator strengths are given in parentheses. The ground state total energies (in hartrees) are given as footnotes. Ground state (gs) total energies (in hartrees): −499.4275695 (MR-CISD/d-aug-DZ); −499.4642611 (MR-CISD+Q/d-aug-DZ); −499.5216686 (MR-CISD/d-aug-TZ);- 499.5677825 (MR-CISD+Q/d-aug-TZ). [b]At the MR-CISD/d-aug-DZ level. [c]MR-CISD+Q taken from reference.[22] [d]Taken from reference.[11] [e]aug-cc-pVDZ(Cl,H)/d-aug-cc-pVDZ(C). [f]aug-cc-pVTZ(Cl,H)/d-aug-cc-pVTZ(C). [g]Oscillator strengths.

→ AUX excitations are allowed. At the MCSCF level, five states (the ground state, one $2p_\sigma3s(C)$, and three $2p_\sigma3p(C)$) have been averaged. For methyl cation, the three σ_{CH} and the $2p_\sigma$ orbitals have been included in the CAS space at both levels, and two states (the ground and the $\sigma_{CH}2p_\sigma$ states) have been averaged at the MCSCF level.

Analytical gradient techniques[46−49] have been employed for all geometry optimizations at the MR-CISD level, including optimization at the crossing seam, which also counted on analytical nonadiabatic coupling vectors.[50,51]

■ RESULTS AND DISCUSSION

The ground state equilibrium geometry, calculated at the MR-CISD level with the aug-cc-pVTZ(H,Cl)/d-aug-cc-pVTZ(C) basis set, is in good agreement with the experimental one.[52] The main difference has been obtained for the C−Cl bond distance, whose calculated value is 1.818 Å, ∼0.042 Å larger than the experimental value. A better agreement can be achieved through the use of more flexible basis sets and/or even more accurate potential energy surfaces (e.g., at the multi-reference averaged quadratic coupled level, MR-AQCC[40]). However, this is not the purpose of the present investigation.

Vertical Excitation Energies. The vertical excitation energies of CH_3Cl, calculated at the experimental geometry, have been previously discussed.[22] In that work, ten singlet states (including the ground state) have been studied, namely: 1^1A_1, 1^1E, 2^1E, 2^1A_1, 3^1E, 1^1A_2, 4^1E, 3^1A_1, 4^1A_1, and 5^1E. Here, the 5^1A_1 state was additionally included and a total of 11 states was obtained. Since slight modifications in the active space and overall computational procedures have been adopted in this work with respect to the previous one, a brief discussion of the state characters and vertical excitation energies is in order.

The correspondences between C_s and C_{3v} symmetries have been double-checked using as criteria both energy and the characters of each state (the latter, defined in terms of the MR-CISD weights of all configurations and adopting a 0.1 cutoff value). The excited states are vertically assigned to the following excitations (only the dominant excitations are reported; a complete description of the characters and weights of each state is given in Table 1): 1^1E ($n_e \rightarrow \sigma^*$); 2^1E ($n_e \rightarrow 3s(C)$); $2^1A_1(n_e \rightarrow 3p_e(C))$; $3^1E(n_e \rightarrow 3p_e(C))$; 1^1A_2 ($n_e \rightarrow 3p_e(C)$); 4^1E ($n_e \rightarrow 3p_e(C)$); 3^1A_1 ($\sigma \rightarrow 3s(C)$); 4^1A_1 ($\sigma \rightarrow 3p_\sigma(C)$); 5^1E ($\sigma \rightarrow 3p_e(C)$); 5^1A_1 ($\sigma_{CH} \rightarrow \sigma^*$). Vertical

excitation energies, obtained at MR-CISD and MR-CISD+Q levels with the aug-cc-pVXZ(H,Cl)/d-aug-cc-pVXZ(C) (X = D,T) basis sets are included in Table 1.

MR-CISD+Q and MR-CISD vertical excitation energy values generally agree within 0.2 eV, except for the 5^1A_1 state, for which an expressive Davidson correction of ca. 1 eV is observed. Excluding the 5^1A_1 state, the root-mean-square deviation (RMSD) between the two levels is 0.1 eV for both basis sets. Consequently, and different from the MR-CISD picture, the 5^1A_1 state is predicted to appear below the 5^1E at the MR-CISD+Q level. This result is probably an artifact, as a high density of states is expected in the region above 10.0 eV[11,22] and only few of the total number of states in this region have been included in the actual calculations[22] due to the very high computational demand. It is worth mentioning that the vertical excitation energies of the last three states are higher than the ionization threshold of 11.29 eV.[11] Results obtained with both basis sets deviate less than 0.3 eV, suggesting that the aug-cc-pVDZ(Cl,H)/d-aug-cc-pVDZ(C) basis set is satisfactory for describing the vertical excitation profile. Including the 5^1A_1 state, the RMSD between MR-CISD results with both basis sets is only 0.04 eV; for MR-CISD+Q it is 0.1 eV. This result supports the subsequent potential energy curves calculations with the aug-cc-pVDZ(Cl,H)/d-aug-cc-pVDZ(C) basis set.

A general agreement between the MR-CISD and MR-CISD+Q results obtained in this work and the experimental data[11] is observed. An excellent agreement is also observed between the actual and the previous results.[22] In fact, all modifications introduced in the active space and general computational procedures do not affect the theoretical results. As a detailed analysis of the vertical excitation energies has already been done,[22] they will not be further discussed.

Potential Energy Curves. Potential energy profiles along the C−Cl internal coordinate have been computed for all states. As expected, the CH_3 fragment geometry smoothly changes from pyramidal to planar geometry along the dissociation curve, and, at the dissociation limit, this fragment is better characterized as having D_{3h} symmetry. Excited states were obtained as vertical excited states at each point. The obtained potential curves are shown in Figure 1.

The ground state curve has a typical dissociation profile for a bonded species. Along this dissociation curve, the character of
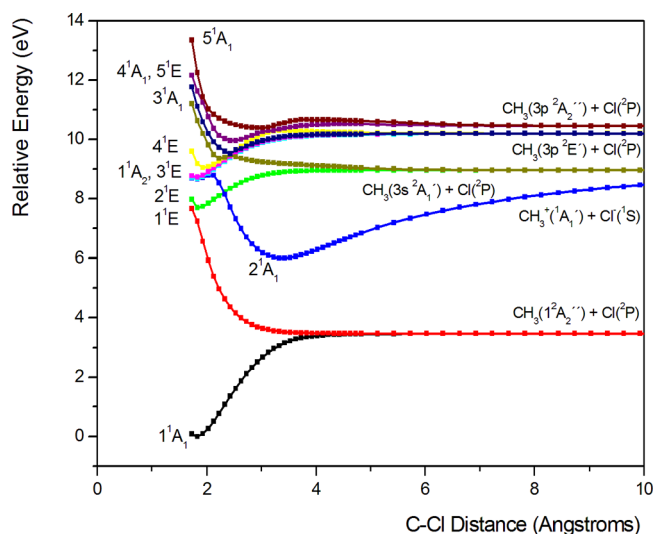
Figure 1. Potential energy curves obtained at the MR-CISD level with the aug-cc-pVDZ(Cl,H)/d-aug-cc-pVDZ (C) basis set.

the molecular orbitals smoothly changes. The σ orbital, for instance, changes to a Cl $n_\sigma(3p_\sigma(Cl))$ orbital, whereas the σ^* orbital becomes the CH_3 $2p_\sigma$ orbital. The main configuration of the lowest state changes from a closed shell, doubly occupied configuration, to the $(n_\sigma(Cl))^1(2p_\sigma(C))^1$ configuration, which better characterizes this state at the dissociation limit. The 1^1E state also changes its character from $n_e\sigma^*$ (which is dominant at the equilibrium geometry) to the $(n_e(Cl))^1(2p_\sigma(C))^1$, accompanying the change on the σ^* orbital character and leading to the same dissociation limit as that observed for the 1^1A_1 curve, namely the $CH_3(\tilde{X}^2A_2'') + Cl(^2P)$ dissociation (see Figure 1).

Four other dissociation limits are observed, which can be assigned to the $CH_3(3s^2A_1') + Cl(^2P)$ (in Figure 1, the 2^1E and 3^1A_1 curves), $CH_3(3p^2E') + Cl(^2P)$ (the 4^1A_1, 3^1E, 4^1E, and 1^1A_2 curves), $CH_3(3p^2A_2'') + Cl(^2P)$ (the 5^1E and 5^1A_1 curves), and the ion-pair state $CH_3^+(^1A_1') + Cl^-(^1S)$ (the 2^1A_1 curve). These dissociation limits are justified by the connection between the dominant configurations assigned vertically at

the equilibrium distance and those obtained for each state at larger displacements (10 Å).

Along the 2^1E curve the main configuration is the n_e3s, evolving into the $(n_e(Cl))^1(3s(C))^1$ configuration at displacements larger than 5 Å, and asymptotically leading to the $CH_3(3s^2A_1') + Cl(^2P)$ dissociation limit. The 3^1A_1 potential curve, for which the $\sigma3s$ character changes to the $(n_\sigma(Cl))^1(3s-(C))^1$ as the C–Cl distance increases, also tends to the same dissociation limit. The 4^1A_1 state changes from $\sigma3p_\sigma$ to the $(n_e(Cl))^1(3p_e(C))^1$ configuration at larger displacements, while the 3^1E and 1^1A_2 states change from n_e3p_e configuration to $(n_e(Cl))^1(3p_e(C))^1$, and the 4^1E changes from n_e3p_σ to $(n_\sigma(Cl))^1(3p_e(C))^1$; all four states go asymptotically to the $CH_3(3p^2E') + Cl(^2P)$ dissociation limit. Finally, the $5^1A_1(\sigma_{CH}\sigma^*)$ and 5^1E ($\sigma3p_e$) states change, respectively, to the $(n_\sigma(Cl))^1(3p_\sigma(C))^1$ and $(n_e(Cl))^1(3p_\sigma(C))^1$ configurations at larger displacements, yielding the $CH_3(3p^2A_2'') + Cl(^2P)$ dissociation limit.

No significant differences are observed for the potential energy profiles calculated at the MR-CISD level with the aug-cc-pVDZ(Cl,H)/d-aug-cc-pVDZ (C) and the aug-cc-pVTZ-(Cl,H)/d″-aug′-cc-pVTZ (C) basis sets, as shown in Figure 2. Minor differences are only observed at the avoided crossing between the 3^1A_1 and 4^1A_1 states, which is slightly higher at the TZ basis set and displaced from ~2.4 Å to 3.0 Å. The TZ profiles also show a nonphysical discontinuity in the 1^1A_2 curve. Small deviations (~0.25 eV) are obtained at the edge of the curves calculated at the MR-CISD level with the aug-cc-pVDZ(Cl,H)/d-aug-cc-pVDZ (C) and the aug-cc-pVTZ-(Cl,H)/d″-aug′-cc-pVTZ (C) basis sets, as can be seen in Figure 2.

Several avoided crossings are observed in these potential curves, yielding changes on the configurations of the states and leading to different photodissociation channels. A detailed discussion of these crossings is done below, based on the results obtained with the aug-cc-pVDZ(Cl,H)/d-aug-cc-pVDZ(C) basis set, for which more points have been calculated.

^1E Curves. The potential energy profiles with emphasis on the ^1E curves are shown in Figure 3. Three main crossings are
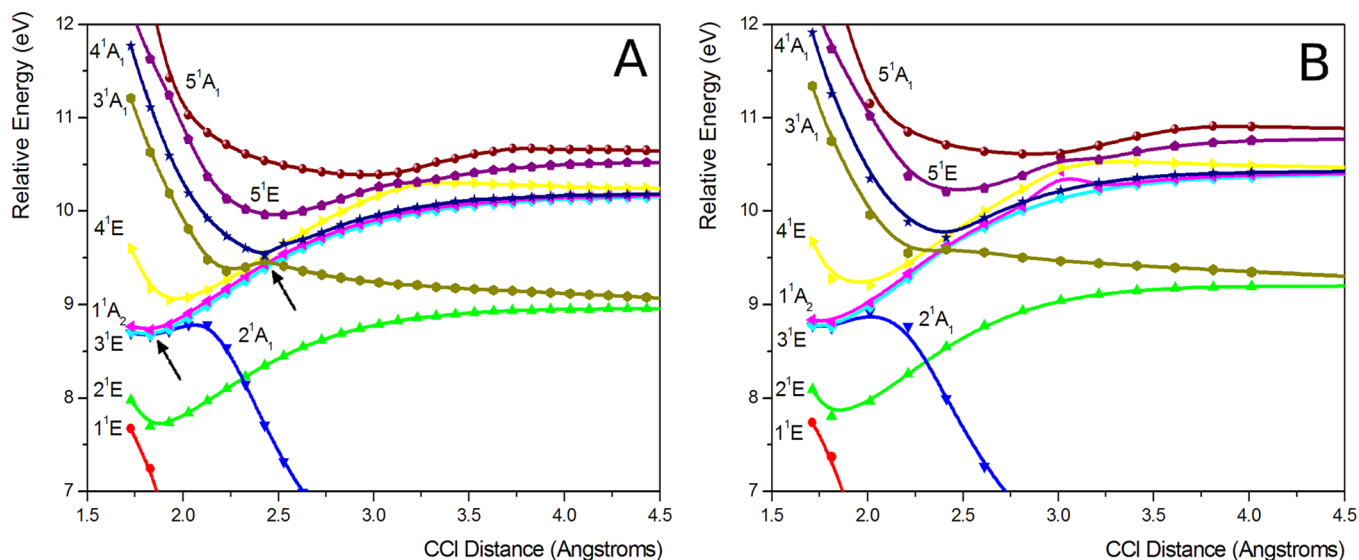

Figure 2. Detailed view of the potential energy curves obtained at the MR-CISD level with (A) aug-cc-pVDZ(Cl,H)/d-aug-cc-pVDZ(C) and (B) aug-cc-pVTZ(Cl,H)/d″-aug′-cc-pVTZ(C) basis sets. The arrows indicate the two geometrical spots with multiple crossings.
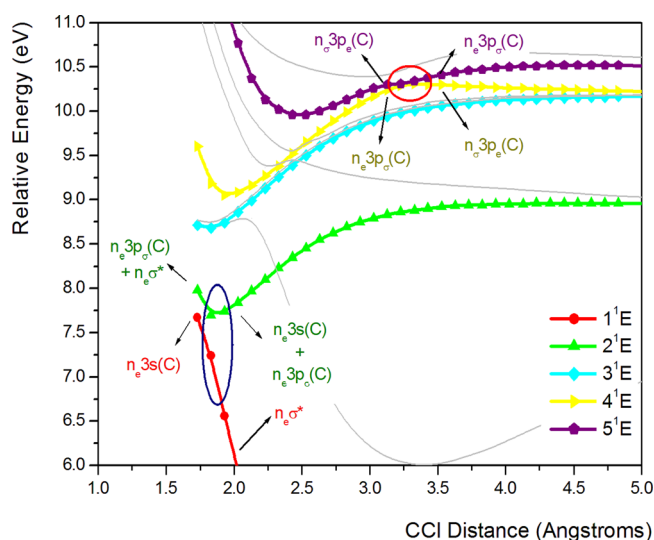
Figure 3. Detailed view of the potential energy curves for the ^1E states, obtained at the MR-CISD level with aug-cc-pVDZ(Cl,H)/d-aug-cc-pVDZ basis set. Configurations involved in the main avoided crossings are indicated.

observed, between the ^1E and 2^1E states at *ca* 1.8 Å, between the 2^1E and 4^1E states at 2.0 Å, and between the 4^1E and 5^1E states at 3.3 Å. Configuration exchanges are indicated for two of these crossings in the figure.

The avoided crossing between the ^1E and 2^1E states is characterized by the exchange between the $n_e\sigma^*$ and $n_e3s(C)$ configurations, with some influence of the $n_e3p_\sigma(C)$ configuration too. As the C–Cl distance increases, the weight of the $n_e3p_\sigma(C)$ configuration decreases in the 2^1E state, which is dominated by the $n_e3s(C)$ configuration from 2.2 Å on.

A large-gap avoided crossing (not explicitly indicated in Figure 3) takes place between the 2^1E and 4^1E states at 2.0 Å, characterized by the exchange between the $n_e3p_\sigma(C)$ and $n_e3s(C)$ configurations. For displacements larger than 2.2 Å, the 4^1E state is better represented by the $n_e3p_\sigma(C)$ configuration. This configuration can be viewed as a contaminating configuration in the 1^1E and 2^1E states, which can be justified on symmetry grounds. The final $n_e\sigma^*$ and $n_e3s(C)$ configurations for the 1^1E and 2^1E states are responsible for the $CH_3(\tilde{X}^2A_2'') + Cl(^2P)$ and $CH_3(3s^2A_1') + Cl(^2P)$ dissociation channels (see Figure 1). Additional details concerning the configurations around the $1^1E/2^1E$ and $2^1E/4^1E$ avoided crossings are given in the Supporting Information.

In the avoided crossing between the 4^1E and 5^1E states, the (n_e3p_σ) and $(n_\sigma3p_e)$ dominant configurations are interchanged. After the avoided crossing, the 4^1E curve (now with the dominant $(n_\sigma3p_e)$ configuration) dissociates as $CH_3(3p^2E') + Cl(^2P)$ and the 5^1E curve (n_e3p_σ) yields (along with the 5^1A_1 state) the $CH_3(3p^2A_2'') + Cl(^2P)$ channel (see Figure 1).

Jahn–Teller Effect in the 1^1E and 2^1E States. As discussed above, an avoided crossing between the 1^1E and 2^1E states takes place at 1.8 Å, slightly before the equilibrium distance (see Figure 3). As both states have E representation, they are subject to the Jahn–Teller effect. Excitation to the 1^1E state, which at the equilibrium geometry corresponds to an $n\sigma^*$ state, should induce symmetry-breaking vibrational movements, lowering the symmetry from C_{3v} to C_s.[11] However, both $2^1A'$ and $1^1A''$ states are highly repulsive along the C–Cl coordinate. Thus, departure from C_{3v} symmetry hardly affects the $CH_3 + Cl$

dissociation channel, as at very large distances the degeneracy is recovered. Besides, it is clear from Figure 1 that they also become degenerate with the $1^1A'$ state due to the equivalence between the three Cl lone pairs orbitals.

On the other hand, the Jahn–Teller effect in the 2^1E (n3s) state may play a different role in the appearance of the $CH_3 + Cl$ dissociation channel. As in the case of 1^1E state, vertical excitation to 2^1E also leads to C_s symmetry. Consequently, an energy splitting of the $^1A'$ and $^1A''$ components of both 1^1E and 2^1E states can yield a crossing between the $3^1A'$ and $1^1A''$ states, as at C_{3v} symmetry the energy difference between the 1^1E and 2^1E states is already small (~0.3 eV, see Figure 3). Such crossing is actually a conical intersection which, after full geometry optimization, leads to the structure shown in the Supporting Information, where it is discussed in detail.

$^1A_1$ Curves. Figure 4 delivers a detailed view of the $^1A_1$ potential energy curves. Avoided crossings between the 2^1A_1
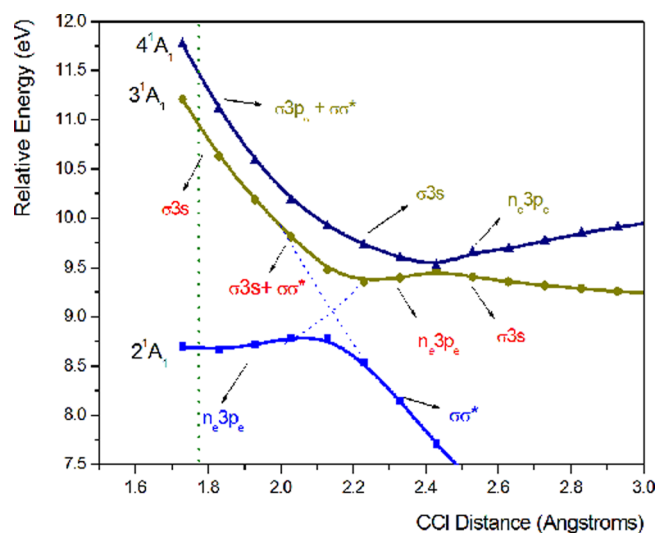

Figure 4. Detailed view of the potential energy curves for the $^1A_1$ states, obtained at the MR-CISD level with aug-cc-pVDZ(Cl,H)/d-aug-cc-pVDZ basis set. An avoided crossing is indicated by dotted lines. The vertical dotted line indicates the $^1A_1$ states at the experimental C–Cl distance.

and 3^1A_1 and between the 3^1A_1 and 4^1A_1 states are observed around 2.1 and 2.4 Å, respectively.

At 1.7 Å, the dominant configurations of the 4^1A_1, 3^1A_1, and 2^1A_1 states are $\sigma3p_\sigma$, $\sigma3s$, and n_e3p_e, respectively, although the former also shows minor contribution of the $\sigma\sigma^*$ excitation. The first observed change of configurations is between the 4^1A_1 and 3^1A_1 states (around 1.9 Å), where the weight of the $\sigma\sigma^*$ excitation increases in the wave function of the 3^1A_1 state. An avoided crossing is then observed between the 3^1A_1 and 2^1A_1 states around 2.1 Å, from which the $\sigma\sigma^*$ character is transferred to the 2^1A_1 state. Moreover, around 2.4 Å, the 3^1A_1 and 4^1A_1 states exchange characters again, the former gaining $(n_\sigma(Cl))^1(3s(C))^1$ character, whereas the latter becomes a n_e3p_e state, which originally was the main component of the 2^1A_1 state.

The $\sigma\sigma^*$ character remains dominant in the 2^1A_1 state up to approximately 2.6 Å (not shown in Figure 4), where the closed shell configuration, formerly observed in the 1^1A_1 (ground state), mixes with the $\sigma\sigma^*$ excitation. A broad avoided crossing is observed between these states. In the region from 2.7–3.0 Å, the shapes and characters of orbitals are also changing, from the

σ and σ^* molecular orbitals to Cl $n_\sigma(3p_\sigma(Cl))$ and $2p_\sigma(CH_3)$ orbitals. The $\sigma\sigma^*$ and the closed shell configurations are, in this region, better characterized as $(n_\sigma(Cl))^1(2p_\sigma(CH_3))^1$ and $(n_\sigma(Cl))^2(2p_\sigma(CH_3))^0$, respectively. After the avoided crossing, these are the dominant configurations in 1^1A_1 and 2^1A_1 states, leading to the homolytic ground state dissociation (curve 1^1A_1 in Figure 1) and to the $CH_3^+\cdots Cl^-$ complex formation (as it will be discussed later), which further dissociates into CH_3^+ and Cl^- ions (curve 2^1A_1 in Figure 1).

At very large distances ($\sim$15 Å) there is an avoided crossing between the 2^1A_1 and 3^1A_1 states. Thus, after 15 Å, one has 2^1E and 2^1A_1 dissociating as $CH_3(3s^2A_1') + Cl(^2P)$, while 3^1A_1 correlates with the $CH_3^+(^1A_1') + Cl^-(^1S)$ dissociation channel (see Table 2 and Figure 5).

Table 2. Dissociation Limits Calculated at the MR-CISD+Q Level with the Mixed aug-cc-pVTZ (Cl,H)/d-aug-cc-pVTZ(C) Basis Set[a]

		dissociation limits	
bound states	dissociation channel	MR-CISD +Q	reference value[b]
1^1A_1, 1^1E	$CH_3(\tilde{X}^2A_2'') + Cl(^2P)$	3.70	3.84
2^1E, 2^1A_1	$CH_3(3s^2A_1') + Cl(^2P)$	9.50	9.70
3^1A_1	$CH_3^+(^1A_1') + Cl^-(^1S)$	10.08	10.07
1^1A_2, 3^1E, 4^1E, 4^1A_1	$CH_3(3p^2E') + Cl(^2P)$	10.76	10.79
5^1E, 5^1A_1	$CH_3(3p^2A_2'') + Cl(^2P)$	11.01	11.21

[a]All values are expressed in eV. [b]See text for details.

Dissociation Limits. Dissociation limits were determined from the potential curves extended to 50 Å, relative to the calculated ground state energy at the experimental geometry. This large displacement was adopted to guarantee a negligible interaction between the fragments, which is especially important for the ionic dissociation limit due to the Coulomb attractive potential. Nevertheless, the relative energy for the latter (taken from the potential energy curve) was further corrected by the R^{-1} Coulomb term (which is 0.29 eV at 50 Å).

The ground state dissociation energy has been determined by Chen and co-workers as 3.59 eV.[53] The CH_3Cl and CH_3

vibrational zero point energies (ZPE), as computed at MR-CISD level with the aug-cc-pVTZ(Cl,H)/d-aug-cc-pVTZ(C) basis set, are 8544 and 6529 cm^{-1}, respectively, yielding an estimate of 3.84 eV for the corrected ground state dissociation limit. Our calculated dissociation limit, at the MR-CISD+Q level with the mixed aug-cc-pVTZ(Cl,H)/d-aug-cc-pVTZ(C) basis set, is 3.70 eV, which is in very good agreement with the value of 3.84 eV.

The energies of the $CH_3(3s^2A_1') + Cl(^2P)$, $CH_3(3p^2E') + Cl(^2P)$, and $CH_3(3p^2A_2'') + Cl(^2P)$ dissociation channels can be obtained from the vertical excitation energies of the CH_3 radical. These latter energies have been computed by Mebel and Lin as 5.86, 6.95, and 7.37 eV ($\tilde{X}^2A_2'' \rightarrow 3s^2A_1'$, $\tilde{X}^2A_2'' \rightarrow 3p^2E'$, and $\tilde{X}^2A_2'' \rightarrow 3p^2A_2''$, respectively).[33] Later, Bauerfeldt and Lischka reported values of 5.81 and 7.07 eV, at the MR-CISD+Q/d-aug-cc-pVDZ level, for the $\tilde{X}^2A_2'' \rightarrow 3s^2A_1'$ and $\tilde{X}^2A_2'' \rightarrow 3p^2A_2''$ excitations,[54] in good agreement with the aforementioned results.[33] As the most complete set of results has been reported by Mebel and Lin, their values are taken for comparison. By summing their results with the corrected experimental ground state dissociation energy (3.84 eV), the $CH_3(3s^2A_1') + Cl(^2P)$, $CH_3(3p^2E') + Cl(^2P)$, and $CH_3(3p^2A_2'') + Cl(^2P)$ dissociation limits can be predicted as 9.70, 10.79, and 11.21 eV. At the MR-CISD+Q level, our calculated values for the corresponding dissociation limits are 9.50, 10.76, and 11.01 eV, which agree well with the reference values.

Literature data for the CH_3 vertical ionization energy and for the chlorine atom electron affinity were used to predict the reference value for the $CH_3^+(^1A_1') + Cl^-(^1S)$ dissociation limit. The vertical ionization energy of CH_3 has been determined by Houle and Beauchamp as 9.84 eV.[55] The Cl electron affinity, 3.61 eV, was taken from NIST.[56] Using these values along with the corrected ground state dissociation energy (3.84 eV), the ionic dissociation limit is predicted as 10.07 eV, while the calculated value at the MR-CISD+Q level with the aug-cc-pVTZ(Cl,H)/d-aug-cc-pVTZ(C) basis set is 10.08 eV.

The results for dissociation limits and literature data are summarized in Table 2, holding very good agreement with the reference values.
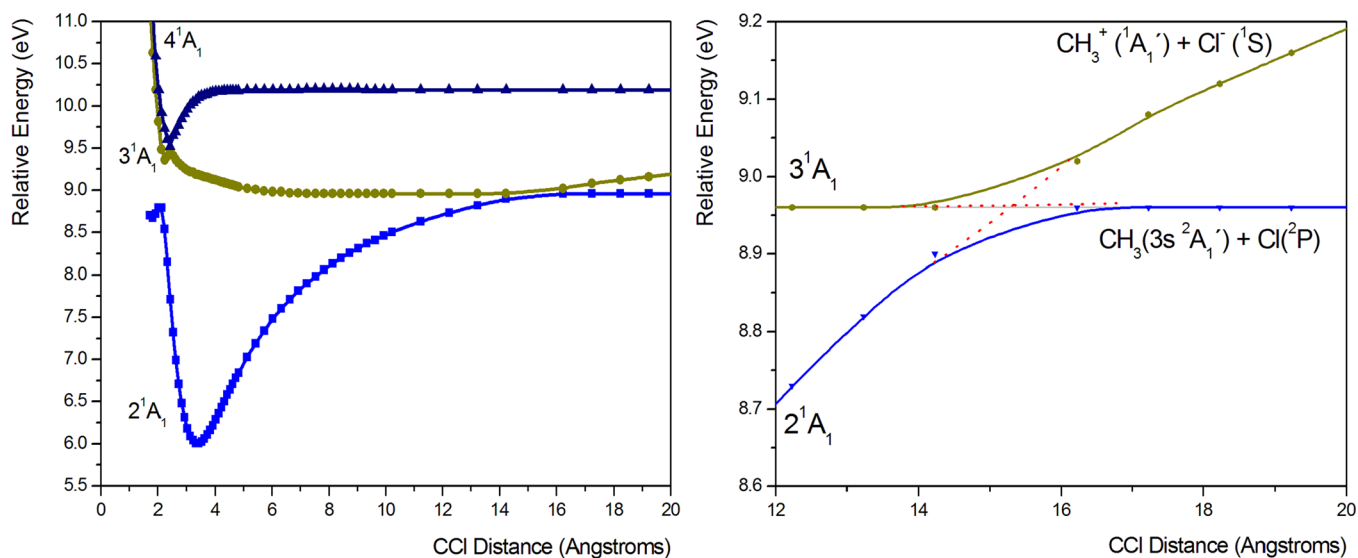

Figure 5. Avoided crossing between the 2^1A_1 and 3^1A_1 states. (A) General overview. (B) Detailed view. The dissociation channels involving these two states are also shown. Before the avoided crossing 2^1E is degenerate with 3^1A_1, while after it becomes degenerate with 2^1A_1 (see Figure 1).

Characterization of the $CH_3^+ \cdots Cl^-$ and $H_2CH^+ \cdots Cl^-$ Complexes. An analysis of the 2^1A_1 curve in Figure 1 suggests that a stationary point correlating with the $CH_3^+ + Cl^-$ dissociation should be found at ca. 3.4 Å. To assess its structure, a full geometry optimization under C_s symmetry restrictions has been performed at the MR-CISD level. It converged to a $CH_3^+ \cdots Cl^-$ electrostatic complex with a C_{3v} geometry in which the C–Cl axis lies perpendicular to the plane containing the CH_3 fragment (the C–Cl distance is 3.298 Å, see Figure 6). This complex is strongly bound by 3.69 eV (MRCI+Q; ZPE corrected) with respect to the $CH_3^+(^1A_1') + Cl^-(^1S)$ dissociation limit.
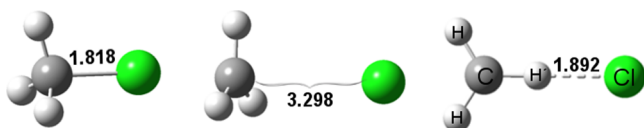

Figure 6. Structures of CH_3Cl ground state (left) and of the $CH_3^+ \cdots Cl^-$ (center) and $H_2CH^+ \cdots Cl^-$ (right) complexes. Bond distance values are in Å. The structures have been obtained at the MR-CISD level with the aug-cc-pVTZ(Cl,H)/d-aug-cc-pVTZ(C) basis set.

A normal-mode analysis showed that this electrostatic complex is not a minimum and has two imaginary frequencies ($322i$ and $321i$ cm^{-1}). After following the normal modes corresponding to those imaginary frequencies, a new geometry optimization revealed the true minimum, a $H_2CH^+ \cdots Cl^-$ complex. This latter complex has C_{2v} symmetry and is also shown in Figure 6. A similar complex was observed for the CH_3F molecule, as reported by Bauerfeldt and Lischka.[54]

In the $H_2CH^+ \cdots Cl^-$ complex, the C–Cl and C–H' distances are 3.044 and 1.152 Å. The ClCH' angle is 0.0°. The C–H distances are 1.082 Å and the HCH and HCH' angles are 116.5° and 121.7°, respectively. The following vibrational wavenumbers were obtained for the $H_2CH^+ \cdots Cl^-$ complex: 3330, 3251, 2346, 1536, 1481, 1425, 796, 434, and 277 cm^{-1}. The Cl–H' distance of 1.892 Å in the complex is much longer than the 1.275 Å of the bound HCl,[57] but much still shorter than 2.95 Å, the sum of van der Waals radii of H and Cl.

At the geometry corresponding to the $CH_3^+ \cdots Cl^-$ electrostatic complex (the minimum of the 2^1A_1 curve in Figure 1), a reasonably high admixture between closed-shell ionic and $\sigma\sigma^*$ configurations has been obtained: $0.59(n_\sigma(Cl))^2 + 0.25\sigma\sigma^*$. However, for the $H_2CH^+ \cdots Cl^-$ complex (which is a minimum in the $3^1A'$ surface), such admixture is significantly reduced: $0.75(n_\sigma(Cl))^2 + 0.11\sigma\sigma^*$. Both species are very polar. In particular, the $H_2CH^+ \cdots Cl^-$ complex has dipole moment of 10.41 D (MR-CISD level) and large charge separation; it can be described as $(H_2CH)^{+\delta} \cdots Cl^{-\delta}$, with $\delta = 0.88$ (from Mulliken's population analysis).

The $H_2CH^+ \cdots Cl^-$ complex lies 4.88 eV above the ground state ($CH_3Cl(1^1A_1)$) and is strongly bound by 4.65 eV (MR-CISD+Q; ZPE corrected) with respect to the $CH_3^+(^1A_1') + Cl^-(^1S)$ dissociation limit. (The total energies of the $H_2CH^+ \cdots Cl^-$ complex at the MR-CISD and MR-CISD+Q levels, with the aug-cc-pVTZ(H,Cl)/d-aug-cc-pVTZ(C) basis set, are −499.3262452 and −499.3809926 hartree, respectively).

The CH⋯Cl Hydrogen Bond. We have seen that along the 2^1A_1 state, a $CH_3^+ \cdots Cl^-$ electrostatically bound complex is formed. Upon rotational relaxation, it gives origin to a $H_2CH^+ \cdots Cl^-$ complex, 0.96 eV more stable. In this latter geometry, the linearity of the CH⋯Cl atoms arrangement

immediately poses the question whether there is a hydrogen bond contributing to hold the $H_2CH^+ \cdots Cl^-$ complex together. This is not a straightforward question to answer first because we are dealing with a ion-pair where the electrostatic attraction naturally overpowers the dipole–induced dipoles; second, we are dealing with electronically excited species; third, as we discuss in the Introduction, CH⋯Cl hydrogen bonds are rare and restricted to molecules very different from that we investigate here.

We have, therefore, tackled the problem from a formal perspective. In 2011, IUPAC has proposed an updated definition of hydrogen bond, flexible enough to encompass the large variety of bonds that lies under this category.[58,59] It has also proposed a series of criteria that a bond should satisfy to be characterized as hydrogen bond. In the Supporting Information, we analyze the CH⋯Cl bond in the $H_2CH^+ \cdots Cl^-$ complex against this definition and each of these criteria, and show that it may be characterized as a hydrogen bond. In fact, to be more precise, the bond holding the $H_2CH^+ \cdots Cl^-$ complex together is primarily a monopole-monopole bond, with additional (strong) stabilization due to an underlying CH⋯Cl hydrogen bond.

All reported cases of CH⋯Cl hydrogen bonds so far take place within sterically restricted environments of crystals and molecular cavities. In the case of the $H_2CH^+ \cdots Cl^-$ complex, the monopole-monopole interaction plays the same role as those steric interactions, holding together the bonded groups allowing the CH⋯Cl stabilization. In terms of the chemical leitmotif described by Gilli and Gilli,[60] this bond can be considered a double-charge assisted hydrogen bond.

Nonadiabatic Relaxation and Formation of Cl^-. The connection between previously reported experimental results related to the ionic dissociation channel and the theoretical results obtained in this work is worthy of attention. As already mentioned, the Cl^- cross section peaks in the region from 10.5−11.9 eV.[23] Moreover, the chloride anion channel was shown to prevail over the appearance of other possible anions. On the basis of the theoretical results, we may propose the following formation mechanism for Cl^-.

The Cl^- elimination should start with photoexcitation of CH_3Cl into the 4^1A_1 state, a bright state with 0.340 oscillator strength and 11.42 eV vertical excitation according to MR-CISD+Q (see Table 1). The system should then quickly relax by stretching the C−Cl distance to 2.5 Å (see Figure 1). There, a cascade of nonadiabatic processes starts, bringing the molecule to lower excited states. From Figure 1, we see that there are two main spots for this nonadiabatic cascade: (1) the multiple crossings between 4^1A_1, 3^1A_1, 4^1E, 1^1A_2, and 3^1E states occurring at ∼2.4 Å; and (2) the multiple crossings between 1^1A_2, 3^1E, and 2^1A_1 states at ∼1.8 Å. These two spots are indicated by arrows in Figure 2A.

Following this deactivation process, all five dissociation channels can be populated. The fraction of the population that ends up in the 2^1A_1 state may form the $CH_3^+ \cdots Cl^-$ electrostatic complex and finally dissociate along the $CH_3^+ + Cl^-$ channel. The $H_2CH^+ \cdots Cl^-$ complex should not be formed because of the large excess of the vibrational energy in the 2^1A_1 state.

The origin of the cross section at 10 eV (see Figure 4(b) from ref 23) matches very well our dissociation limit for the 2^1A_1 ion-pair state (10.08 eV, Table 2). The vibrational structure in this experimental band also indicates that bound states are populated during the predissociation. These bound states should mainly be the 4^1A_1 state (which is initially

photoexcited), along with the 3^1A_1 and 5^1E states. All these three states have clear wells with minima above 9.3 eV (Figure 1). The fading of the vibrational structure at ~11 eV also corroborates this assignment, matching our calculated dissociation limit at 10.76 eV (Table 2). If the bound state were the 4^1E, the spectrum would start at ~9 eV; if it were the 2^1E, we would not see any vibrational progression because of the dissociation limit at 9.5 eV.

Detection of the $H_2CH^+ \cdots Cl^-$ Complex. We have shown that the $H_2CH^+ \cdots Cl^-$ complex is very stable. However, because its minimum geometry is much displaced in relation to the Franck−Condon region, we should not expect a vibrationally resolved band in the absorption spectrum of CH_3Cl around 6 eV, the bottom of 2^1A_1 state. Indeed, no sign of vibrational structure corresponding to this complex can be seen in the experimental absorption spectrum (see, for instance, Figure 2 from ref 21).

Alternatively, the $H_2CH^+ \cdots Cl^-$ complex may be detectable by time-resolved spectroscopy. This is still not trivial because, due to the same displacement of the minimum, it should not be possible to directly excite the 2^1A_1 from the ground state. Therefore, as schematically depicted in Figure 7, the detection of the $H_2CH^+ \cdots Cl^-$ complex may require a sequence of three femtosecond-resolved laser pulses, to indirectly excite and probe the 2^1A_1 state.
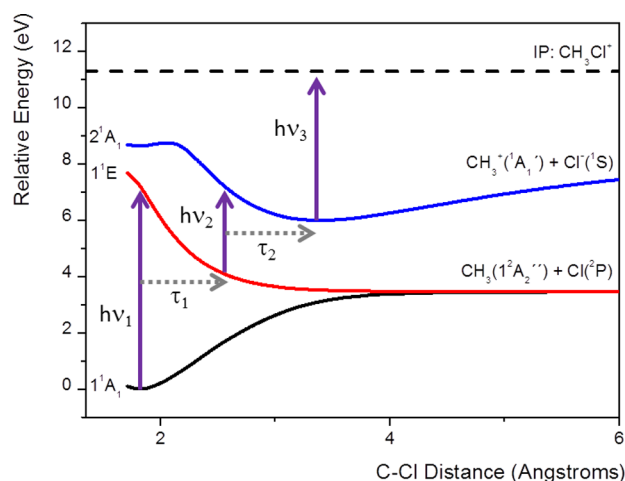

Figure 7. Scheme of a sequence of three time-resolved ultrashort laser pulses for detection of the $H_2CH^+ \cdots Cl^-$ complex. Only the relevant states are shown.

The first pulse ($h\nu_1 \sim 7$ eV) should excite the 1^1E band. After a short delay (τ_1), probably inferior to 100 fs, the second pulse ($h\nu_2 \sim 3$ eV) should populate the 2^1A_1 state, where the $H_2CH^+ \cdots Cl^-$ complex is formed. Finally, the third pulse delayed by τ_2 should ionize the complex. Taking into account that the ionization potential of CH_3Cl is 11.29 eV,[11] a third pulse set to $h\nu_3 \sim 5$ eV will probe only the complex. Such a three pulses scheme should make CH_3Cl a show case for femtosecond 2D Fourier transform spectroscopy.[61]

CONCLUSION

For the first time, highly correlated electronic structure calculations (MR-CISD) have been performed to elucidate the CH_3Cl photodissociation pathways. The yielded potential energy curves, along with complementary energetic data, can be the grounds for a comprehensive assignment and interpretation of the experimental data concerning the electronic states of the generated photofragments.

Five dissociation channels along the C−Cl coordinate have been identified and characterized: (i) $CH_3(\tilde{X}^2A_2'') + Cl(^2P)$, (ii) $CH_3(3s^2A_1') + Cl(^2P)$, (iii) $CH_3^+(^1A_1') + Cl^-(^1S)$, (iv) $CH_3(3p^2E') + Cl(^2P)$, and (v) $CH_3(3p^2A_2'') + Cl(^2P)$. The first channel can be accessed through $n\sigma^*$ and n3s states, while the second channel can be accessed through n_e3s, n_e3p_σ, and $\sigma3s$ states. The third channel, corresponding to an ion-pair formation, is accessed through n_e3p_e states. The fourth is accessed through n_e3p_e, n_e3p_σ, and $\sigma3p_\sigma$, while the fifth through $\sigma3p_e$ and $\sigma_{CH}\sigma^*$ states. Their relative dissociation limits deviate by at most 0.2 eV from previously reported data.

Our theoretical analysis provides a complete rationalization for the nonadiabatic relaxation of CH_3Cl and, in particular, the formation mechanism of Cl^- after photoexcitation. It confirms the assumption made by Rogers et al.[23] that chloride anion is formed indirectly by crossing Rydberg states of the parent molecule until the ion-pair surface is reached. We discuss that there are two geometrical spots at C−Cl distances of 1.8 and 2.4 Å, where multiple state intersections should promote a cascade of nonadiabatic events, bringing the molecule to lower excited states and feeding the diverse channels.

Finally, we show that along the ion-pair state (2^1A_1), a strongly bound $CH_3^+ \cdots Cl^-$ electrostatic complex is formed at C−Cl distance of 3.3 Å. Upon rotational relaxation, this complex is further stabilized by a $CH \cdots Cl$ double-charge-assisted hydrogen bond, giving rise to a $H_2CH^+ \cdots Cl^-$ complex. On the basis of the theoretical results, a three-pulses time-resolved spectroscopic setup is suggested to detect the $H_2CH^+ \cdots Cl^-$ complex.

ASSOCIATED CONTENT

S **Supporting Information**

The Supporting Information is available free of charge on the ACS Publications website at DOI: 10.1021/jacs.5b10573.

Conical intersection between the $n\sigma^*$ and n3s states; analysis of the avoided crossings; analysis of the $CH \cdots Cl$ bond; Cartesian coordinates of all species. (PDF)

AUTHOR INFORMATION

Corresponding Authors
*mario.barbatti@univ-amu.fr
*silmar@quimica.ufpb.br

Notes
The authors declare no competing financial interest.

ACKNOWLEDGMENTS

REFERENCES

(1) Molina, M. J.; Rowland, F. S. *Nature* **1974**, *249*, 810−812.
(2) Rowland, F. S.; Molina, M. J. *Science* **1975**, *190*, 1038.
(3) Khalil, M. A. K. *The Handbook of Environmental Chemistry, Part 4E, Reactive Halogen Compounds in the Atmosphere*; Febian, P., Singh, O. N., Eds.; Springer, 1999.
(4) Hamilton, J. T. G.; McRoberts, W. C.; Keppler, F.; Kalin, R. M.; Harper, D. B. *Science (Washington, DC, U. S.)* **2003**, *301*, 206−209.

(5) Lucena, J. R.; Ventura, E.; do Monte, S. A.; Araújo, R. C. M. U.; Ramos, M. N.; Fausto, R. *J. Chem. Phys.* **2007**, *127*, 164320−164331.

(6) Medeiros, V. C. de; Ventura, E.; do Monte, S. A. *Chem. Phys. Lett.* **2012**, *546*, 30−33.

(7) Granucci, G.; Medders, G.; Maria, A. *Chem. Phys. Lett.* **2010**, *500*, 202−206.

(8) Yen, M.; Johnson, P. M.; White, M. G. *J. Chem. Phys.* **1993**, *99*, 126−139.

(9) Mayor, E.; Velasco, A. M.; Martín, I. *J. Phys. Chem. A* **2004**, *108*, 5699−5703.

(10) Gilbert, R.; Sauvageau, P.; Sandorfy, C. *J. Chem. Phys.* **1974**, *60*, 4820−4824.

(11) Locht, R.; Leyh, B.; Hoxha, A.; Jochims, H. W.; Baumgärtel, H. *Chem. Phys.* **2001**, *272*, 259−275.

(12) Kawasaki, M.; Kasatani, K.; Sato, H.; Shinohara, H.; Nishi, N. *Chem. Phys.* **1984**, *88*, 135−142.

(13) Brownsword, R. A.; Hillenkamp, M.; Laurent, T.; Vatsa, R. K.; Volpp, H.-R.; Wolfrum, J. *J. Chem. Phys.* **1997**, *106*, 1359−1366.

(14) Matsumi, Y.; Das, P. K.; Kawasaki, M. *J. Chem. Phys.* **1992**, *97*, 5261−5261.

(15) Matsumi, Y.; Das, P. K.; Kawasaki, M. *J. Chem. Phys.* **1990**, *92*, 1696−1701.

(16) Matsumi, Y.; Tonokura, K.; Kawasaki, M.; Inoue, G.; Satyapal, S.; Bersohn, R. *J. Chem. Phys.* **1991**, *94*, 2669−2674.

(17) Tonokura, K.; Matsumi, Y.; Kawasaki, M.; Kasatani, K. *J. Chem. Phys.* **1991**, *97*, 5065−5071.

(18) Tonokura, K.; Mo, Y.; Matsumi, Y.; Kawasaki, M. *J. Phys. Chem.* **1992**, *96*, 6688−6693.

(19) Lin, J. J.; Chen, Y.; Lee, Y. Y.; Lee, Y. T.; Yang, X. *Chem. Phys. Lett.* **2002**, *361*, 374−382.

(20) Amaral, G.; Xu, K.; Zhang, J. *J. Phys. Chem. A* **2001**, *105*, 1115−1120.

(21) Eden, S.; Limão-Vieira, P.; Hoffmann, S. V.; Mason, N. J. *Chem. Phys.* **2007**, *331*, 232−244.

(22) De Medeiros, V. C.; do Monte, S. A.; Ventura, E. *RSC Adv.* **2014**, *4*, 64085−64092.

(23) Rogers, N. J.; Simpson, M. J.; Tuckett, R. P.; Dunn, K. F.; Latimer, C. J. *Phys. Chem. Chem. Phys.* **2010**, *12*, 10971−10980.

(24) Simpson, M. J.; Tuckett, R. P. *Int. Rev. Phys. Chem.* **2011**, *30*, 197−273.

(25) Zhong, Y. R.; Cao, M. L.; Mo, H. J.; Ye, B. H. *Cryst. Growth Des.* **2008**, *8*, 2282−2290.

(26) Thallapally, P. K.; Nangia, A. *CrystEngComm* **2001**, *3*, 114−119.

(27) Taylor, R.; Kennard, O. *J. Am. Chem. Soc.* **1982**, *104*, 5063−5070.

(28) Aakeroy, C. B.; Evans, T. A.; Seddon, K. R.; I, P. *New J. Chem.* **1999**, *23*, 145−152.

(29) Yamabe, S.; Yamazaki, S. *J. Phys. Org. Chem.* **2009**, *22*, 1094−1103.

(30) Li, Y.; Flood, A. H. *Angew. Chem., Int. Ed.* **2008**, *47*, 2649−2652.

(31) Tresca, B. W.; Zakharov, L. N.; Carroll, C. N.; Johnson, D. W.; Haley, M. M. *Chem. Commun.* **2013**, *49*, 7240−7242.

(32) Antol, I.; Eckert-Maksić, M.; Müller, T.; Dallos, M.; Lischka, H. *Chem. Phys. Lett.* **2003**, *374*, 587−593.

(33) Mebel, A. M.; Lin, S. *Chem. Phys.* **1997**, *215*, 329−341.

(34) Bunge, A. *J. Chem. Phys.* **1970**, *53*, 20−28.

(35) Langhoff, S. R.; Davidson, E. R. *Int. J. Quantum Chem.* **1974**, *8*, 61−72.

(36) Bruna, P. J.; Peyerimhoff, S. D.; Buenker, R. J. *Chem. Phys. Lett.* **1980**, *72*, 278−284.

(37) Lischka, H.; Shepard, R.; Brown, F. B.; Shavitt, I. *Int. J. Quantum Chem.* **1981**, *15*, 91.

(38) Shepard, R.; Shavitt, I.; Pitzer, R. M.; Comeau, D. C.; Pepper, M.; Lischka, H.; Szalay, P. G.; Ahlrichs, R.; Brown, F. B.; Zhao, J. *Int. J. Quantum Chem.* **1988**, *22*, 149−165.

(39) Lischka, H.; Shepard, R.; Shavitt, I.; Pitzer, R. M.; Dallos, M.; Müller, T.; Szalay, P. G.; Brown, F. B.; Ahlrichs, R.; Böhm, H. J.; Chang, A.; Comeau, D. C.; Gdanitz, R.; Dachsel, H.; Ehrhardt, C.; Ernzerhof, M.; Höchtl, P.; Irle, S.; Kedziora, G.; Kovar, T.; Parasuk, V.;

Pepper, M. J. M.; Scharf, P.; Schiffer, H.; Schindler, M.; Schüler, M.; Seth, M.; Stahlberg, E. A.; Zhao, J.-G.; Yabushita, S.; Zhang, Z.; Barbatti, M.; Matsika, S.; Schuurmann, M.; Yarkony, D. R.; Brozell, S. R.; Beck, E. V; Blaudeau, J.-P.; Ruckenbauer, M.; Sellner, B.; Plasser, F.; Szymczak, J. J. *COLUMBUS, an Ab-Initio Electronic Structure Program*, release 7.0, 2012, www.univie.ac.at/columbus accessed on December 16, 2015.

(40) Lischka, H.; Shepard, R.; Pitzer, R. M.; Shavitt, I.; Dallos, M.; Müller, T.; Szalay, P. G.; Seth, M.; Kedziora, G. S.; Yabushita, S.; Zhang, Z. *Phys. Chem. Chem. Phys.* **2001**, *3*, 664−673.

(41) Helgaker, T.; Jensen, H. J. A.; Jørgensen, P.; Olsen, J.; Ruud, K.; Agren, H.; Andersen, T.; Bak, K. L.; Bakken, V.; Christiansen, O.; Dahle, P.; Dalskov, E. K.; Enevoldsen, T.; Fernandez, B.; Heiberg, H.; Hettema, H.; Jonsson, D.; Kirpekar, S.; Kobayashi, R.; Koch, H.; Mikkelsen, K. V.; Norman, P.; Packer, M. J.; Saue, T.; Taylor, P. R.; Vahtras, O., *DALTON, an Ab-Initio Electronic Structure Program*, release 1.0, 1997, www.daltonprogram.org accessed on December 16, 2015.

(42) Dunning, T. H. *J. Chem. Phys.* **1989**, *90*, 1007−1023.

(43) Dunning, T.H. J.; Peterson, K. A.; Wilson, A. K. *J. Chem. Phys.* **1993**, *98*, 1358−1371.

(44) Kendall, R., Jr.; Dunnin, T.; Harrison, R. *J. Chem. Phys.* **1992**, *96*, 6796−6806.

(45) Woon, D. E.; Dunning, T. H., Jr. *J. Chem. Phys.* **1994**, *100*, 2975−2988.

(46) Shepard, R. *Int. J. Quantum Chem.* **1987**, *31*, 33−44.

(47) Shepard, R.; Lischka, H.; Szalay, G. P.; Kovar, T.; Ernzerhof, M. *J. Chem. Phys.* **1992**, *96*, 2085−2098.

(48) Shepard, R. In *Modern Electronic Structure Theory Part I*; Yarkony, D. R., Ed.; World Scientific: Singapore, 1995; p 345.

(49) Lischka, H.; Dallos, M.; Shepard, R. *Mol. Phys.* **2002**, *100*, 1647−1658.

(50) Lischka, H.; Dallos, M.; Szalay, P. G.; Yarkony, D. R.; Shepard, R. *J. Chem. Phys.* **2004**, *120*, 7322−7329.

(51) Dallos, M.; Lischka, H.; Shepard, R.; Yarkony, D. R.; Szalay, P. G. *J. Chem. Phys.* **2004**, *120*, 7330−7339.

(52) Jensen, P.; Brodersen, S.; Guelavich, G. *J. Mol. Spectrosc.* **1981**, *88*, 378−393.

(53) Chen, E. C. M.; Albyn, K.; Dussack, L.; Wentworth, W. E. *J. Phys. Chem.* **1989**, *93*, 6827−6832.

(54) Bauerfeldt, G. F.; Lischka, H. *J. Phys. Chem. A* **2004**, *108*, 3111−3118.

(55) Houle, F. A.; Beauchamp, J. L. *J. Am. Chem. Soc.* **1979**, *101*, 4067−4074.

(56) NIST Computational Chemistry Comparison and Benchmark Database NIST Standard Reference Database Number 101 Release 16a, August 2013, Editor: Russell D. Johnson III. http://cccbdb.nist.gov/ accessed at December 16, 2015.

(57) Huber, K. P.; Herzberg, G. *Molecular Spectra and Molecular Structure. IV. Constants of Diatomic Molecules*; van Nostrand Reinhold Co: New York, 1979.

(58) Arunan, E.; Desiraju Gautam, R.; Klein Roger, A.; Sadlej, J.; Scheiner, S.; Alkorta, I.; Clary David, C.; Crabtree Robert, H.; Dannenberg Joseph, J.; Hobza, P.; Kjaergaard Henrik, G.; Legon Anthony, C.; Mennucci, B.; Nesbitt, D. *Pure Appl. Chem.* **2011**, *83*, 1619−1636.

(59) Arunan, E.; DesirajuGautam, R.; Klein Roger, A.; Sadlej, J.; Scheiner, S.; Alkorta, I.; Clary David, C.; Crabtree Robert, H.; Dannenberg Joseph, J.; Hobza, P.; Kjaergaard Henrik, G.; Legon Anthony, C.; Mennucci, B.; Nesbitt, D. *Pure Appl. Chem.* **2011**, *83*, 1637−1641.

(60) Gilli, P.; Gilli, G. *J. Mol. Struct.* **2010**, *972*, 2−10.

(61) Jonas, D. M. *Annu. Rev. Phys. Chem.* **2003**, *54*, 425−463.